Trace doping of early transition metal enabled efficient and durable oxygen reduction catalysis on Pt-based ultrathin nanowires

Lei Gao [a,1], Tulai Sun [b,1], Xin Tan [c,1], Maochang Liu [d,*], Fei Xue [d], Bin Wang [d,*], Jiawei Zhang [a], Yang-Fan Lu [e], Chao Ma [a], He Tian [e], Shengchun Yang [d], Sean C. Smith [c], Hongwen Huang [a,f,**]

[a] College of Materials Science and Engineering, Hunan Joint International Laboratory of Advanced Materials and Technology for Clean Energy, Hunan University, Changsha, Hunan 410082, PR China
[b] Center for Electron Microscopy, State Key Laboratory Breeding Base of Green Chemistry Synthesis Technology and College of Chemical Engineering, Zhejiang University of Technology, Hangzhou, Zhejiang 310014, PR China
[c] Integrated Materials Design Laboratory, Department of Applied Mathematics, Research School of Physics, The Australian National University, Canberra, ACT 2601, Australia
[d] International Research Center for Renewable Energy, State Key Laboratory of Multiphase Flow in Power Engineering, School of Physics, MOE Key Laboratory for Non-equilibrium Synthesis and Modulation of Condensed Matter, State Key Laboratory for Mechanical Behavior of Materials, Xi'an Jiaotong University, Xi'an, Shanxi 710049, PR China
[e] State Key Lab of Silicon Materials, School of Materials Science and Engineering, Zhejiang University, Hangzhou, Zhejiang 310027, PR China
[f] Hefei National Laboratory for Physical Sciences at the Microscale, University of Science and Technology of China, Hefei, Anhui 230026, PR China

ARTICLE INFO

ABSTRACT

Discovering an active and durable catalyst for oxygen reduction reaction is crucial to the commercialization of fuel cells, but remains grand challenging. Here we report, for the first time, the trace doping of early transition metal (ETM) Re into ultrathin PtNiGa nanowires (Re-PtNiGa NWs) to construct a novel catalyst integrating the superior activity, long-time durability, and high utilization efficiency of Pt atoms. Impressively, the Re-PtNiGa tetrametallic NWs present a 19.6-fold enhancement in mass activity (3.49 A mg^{-1}_{Pt}) compared to commercial Pt/C catalyst and only a 10.6% loss in mass activity after 20,000 cycles of durability test. Moreover, the real fuel cell assembled by Re-PtNiGa NWs on the cathode strongly supports its great potential in fuel cells. The density functional theory calculations reveal that introduction of ETM Re into PtNiGa NWs could weaken binding strength of oxygenated species and elevate dissolution potential, well rationalizing the great enhancements in activity and durability.

1. Introduction

As an ideal power source for transportation vectors, the proton exchange membrane fuel cells (PEMFCs) have received enormous attention from the academical and industrial communities [1–4]. However, the high cost of associated devices arising from the use of a large amount of precious Pt-based electrocatalyst, which compensates the insufficient activity toward oxygen reduction reaction (ORR) on the cathode and long-term operation durability to ensure the desired performance, retards the largescale deployment of the devices [5,6]. To reduce the loading of Pt-based electrocatalysts, exploring the electrocatalysts with

simultaneously improved mass activity and catalytic stability is the best choice at present.

To this aim, great research efforts had been made in optimizing the geometrical factors and chemical environment via constructing the favorable architectures (e.g., facet-engineered structure, core-shell structure, hollow/open structure, and ultrathin low-dimensional structure) and forming alloys [7–26]. Based on these strategies, it had been well-demonstrated that Ga-doped PtNi octahedral nanoparticles (Ga-PtNi) possessed excellent ORR performance by shaping the favorable (111) facets and optimizing elemental composition, exhibiting 11.7-fold increasement in mass activity compared to Pt/C and 88%

retention in mass activity after 15,000 cycles [27]. Despite the considerable stride for Ga-PtNi/C, further improvements in the Pt utilization efficiency (UE), activity and durability are imperative to achieve full-scale commercialization of PEMFCs. To increase the UE of Pt atoms and reduce its usage, one-dimensional (1D) ultrathin Pt-based nanowires (NWs) with a less than 2 nm in diameter have shown great promise to address the issue [28–34]. Besides, the 1D Pt-based ultrathin NWs generally present the improved catalytic durability because of the improved resistance to the detachment from carbon support originating from the strengthened interaction between Pt ultrathin NWs with carbon support [16,28,33–36]. As for activity and durability designs, alloying minute amount of early transition metal (ETM including Mo, Cr, W, Y, Nb, etc.) with Pt to form Pt-based alloys is an effective method, which concurrently improves ORR activity and durability of catalysts [22,23, 37–40], especially given the improvement of stability by this strategy. In term of the above analysis, trace doping of ETM into Pt-based ultrathin NWs is of great interest and importance, which would offer new opportunities to find active and durable ORR electrocatalysts for widespread application of PEMFCs, but has been scarcely reported so far.

Herein we report the design of a catalyst by doping the ETM Re, which be expected to further improve the ORR durability given its unique chemical stability and high melting point [41,42], into ultrathin PtNiGa NWs for the first time. Indeed, the synthesized one-nanometer-thin Re-PtNiGa tetrametallic NWs possess a top-level ORR performance, presenting a 19.6-fold enhancement in mass activity compared to commercial Pt/C catalyst and only a 10.6% loss in mass activity after 20,000 cycles of durability test. More impressively, the real fuel cell assembled by Re-PtNiGa NWs on the cathode delivers excellent activity (961 mW cm^{-2} for Re-PtNiGa tetrametallic NWs versus 702 mW cm^{-2} for Pt/C catalyst under close Pt loading amount) and long-term durability (4.9% decay after 100 h of durability test), strongly supporting the great potential of Re-PtNiGa tetrametallic catalyst for fuel cell. The density functional theory (DFT) calculations are also performed to testify the experimental observations in activity and durability and understand the roles of incorporated Re atoms.

2. Experimental section

2.1. Chemicals

Platinum (II) acetylacetonate (Pt(acac)$_2$, 97%), nickel (II) acetylacetonate (Ni(acac)$_2$, 97%), gallium (III) acetylacetonate (Ga(acac)$_3$, 97%), ammonium perrhenate (VII) (NH$_4$ReO$_4$, 99%), cetyltrimethylammonium bromide (CTAB, 99%), tungsten hexacarbonyl (W (CO)$_6$, 97%), oleylamine (OAm, 70%) and Nafion (5 wt%) were purchased from Sigma-Aldrich. Ethanol (CH$_3$CH$_2$OH, 99%) and perchloric acid (HClO$_4$, 70–72%) were purchased from Sinopharm Chemical Reagent Co. Ltd. (Shanghai, China). The water (18.2 MΩ/cm) were freshly prepared through an ultra-pure purification system (Master-515Q, HHitech). All the chemicals were used without further purification.

2.2. Synthesis of ultrathin Pt-based nanowires

In a typical synthesis of ultrathin Re-PtNiGa NWs, Pt(acac)$_2$ (20.0 mg), Ni(acac)$_2$ (10.0 mg), Ga(acac)$_3$ (11.0 mg), NH$_4$ReO$_4$ (2.4 mg), CTAB (75.0 mg), and 4 mL OAm were added into a 30 mL glass vial. After sonicated for 30 min, W(CO)$_6$ (20.0 mg) was added into the predispersed solution and capped. The resulting homogeneous mixture was then heated and kept at 170 °C for 2 h in an oil bath, which were collected by centrifugation at 13,000 rpm and cleaned four times with a hexane/ethanol mixture (v/v = 2/1), then dried under vacuum. The preparation of other ultrathin Pt-based nanostructures was similar to that of Re-PtNiGa NWs except that Ni(acac)$_2$, Ga(acac)$_3$ and NH$_4$ReO$_4$ were replaced by desired metal salt precursors and reaction temperature was changed. The detailed synthetic parameters for other Pt-based NWs have been listed in Table S1.

2.3. Characterization techniques

Powder X-ray diffraction (XRD) patterns were collected to analyze the crystal structures of NWs by X-ray diffractometer (Rigaku Miniflex-600) with a Cu Kα radiation (λ = 0.15406 nm, 40 kV). Transmission electron microscopy (TEM) images were carried out on a JEOL 2100-Plus operating at 120 kV with the samples deposited on carbon-coated copper TEM grids. HAADF-STEM images, EDS line-scan file were taken on a JEOL ARM-200F microscope with spherical aberration corrector operating at 200 kV. Elemental analysis of ultrathin NWs was quantitatively determined by ICP-AES with a SPECTRO BLUE SOP. The XPS spectrum was collected using an Escalab 250Xi equipped with an Al Ka (1486.6 eV) excitation source. All the spectra collected were corrected using a Shirley background. Compositions were determined by considering the atomic sensitivity factors. Center of gravity calculation for the valence band spectra is conducted as $\frac{\int N(\varepsilon)\varepsilon d\varepsilon}{\int N(\varepsilon)d\varepsilon}$ in the range of 0 to − 9.0 eV, where $N(\varepsilon)$ is the density of states.

2.4. Preparation of working electrode

For different NWs/C catalysts, 4 mg of the prepared NWs was added in a chloroform solution (8.0 mL) and sonicated for 1 h. The above dispersed solution was dropwise added to an ethanol solution containing 16 mg of carbon support (Vulcan XC-72) under vigorous stirring for 30 min. After centrifugation and washed twice with hexanes by centrifugation (10,000 rpm), the NWs/C catalysts were re-dispersed in acetic acid and then heated at 70 °C for 12 h to remove the surfactants on the surface of NWs. A certain amount of as-obtained catalyst was mixed with 0.5 mL isopropanol, 0.495 mL ethanol and 0.005 mL Nafion (5 wt%) and sonicated for 1 h to form the homogenously mixed catalyst ink solution. For the commercial Pt/C catalysts (20 wt% loading on Vulcan XC-72 carbon support, Johnson Matthey), the ink solution (2 mg/mL) was prepared and sonicated for 1 h. Finally, prepared catalyst ink was dropped onto the glassy carbon rotating disk electrode (GC, RDE with geometric area of 0.196 cm^2) with the loading amount of Pt at 2.4 μg, 2.3 μg, 2.5 μg, 2.4 μg, and 4.0 μg for Re-PtNiGa NWs/C, PtNiGa NWs/C, PtNi NWs/C, Pt NWs/C, and commercial Pt/C catalysts, respectively (based on ICP-AES).

2.5. Membrane electrode assembly (MEA) fabrication and single-cell test

The catalysts activity was evaluated under PEMFC operating conditions. Specifically, Re-PtNiGa NWs/C, PtNiGa NWs/C, and commercial Pt/C were employed as the cathode catalysts and Pt/C (20 wt% loading, Johnson Matthey) was used for the anode. Catalysts (5 mg) were mixed with isopropanol (1.16 mL), deionized water (289 μL), and Nafion alcohol solution (54 μL) to prepare the ink, which contained the Nafion ionomer-to-catalyst weight ratio of 0.50. The active area of electrodes was 5 cm^2. The formed catalyst ink was prepared by ultrasonicating for 1 h and sprayed directly onto a carbon paper (HCP120). The Pt loading at the cathode was 0.14 mg$_{Pt}$ cm^{-2} for Re-PtNiGa NWs, 0.15 mg$_{Pt}$ cm^{-2} for PtNiGa NWs, and 0.16 mg$_{Pt}$ cm^{-2} for commercial Pt/C, respectively. As for the anode, Pt/C was used with a loading of 0.14 mg$_{Pt}$ cm^{-2}. The H2-O2 fuel cells were tested (SMART2PEMDM) under galvanic mode using humidified H2 and O2 gases. The cell temperature was set to 80 °C, and the flow rate of both H2 and O2 (1 bar of backpressure) gases was 300 mL/min and 600 mL/min.

2.6. Electrochemical testing

Electrochemical tests were conducted using a three-electrode cell on a CHI760e electrochemical work station (Chenhua Instrument, China). A glassy carbon Rotating Disk Electrode (RDE, diameter: 5 mm) was used as the working electrode, the Ag/AgCl (3 M KCl) electrode was used as a reference electrode, and a platinum wire was used as a counter

electrode. All potentials were converted to the reversible hydrogen electrode reference. The cyclic voltammograms (CVs) were tested in a N$_2$-saturated 0.1 M HClO$_4$ electrolyte with a sweep rate of 50 mV s^{-1}. The electrochemical active surface areas (ECSAs) were calculated by integrating the hydrogen adsorption/desorption charge area between 0.05 and 0.38 V$_{RHE}$ from the CVs. The equation for the calculation of ECSAs was shown as follows:

$$\text{ECSA}_{\text{Pt,cat}}\left(m^2\big/g_{\text{Pt}}\right) = \left[\frac{Q_{\text{H–adsorption}}(C)}{210\ \mu C\big/cm^2 L_{\text{Pt}}(mg_{\text{Pt}}/cm^2)A_{\text{g}}(cm^2)}\right] \times 10^5$$

The charge density for the adsorption of one monolayer hydrogen on Pt (Q$_H$) was assumed to be 210 μC cm^{-2}. L$_{Pt}$ (mg$_{Pt}$/cm^2) was the working electrode Pt loading. A$_g$ (cm^2) was the geometric surface area of the glassy carbon electrode (0.196 cm^2). For CO stripping measurements, CO gas (99.99%) was fed into the electrolyte with holding a potential of 0.1 V$_{RHE}$ for 30 min. Then, N2 gas was purged to remove CO from the electrolyte, and the CO stripping curves were recorded between 0.05 and 1.10 V$_{RHE}$ with a sweep rate of 50 mV s^{-1}. The charge density for the monolayer adsorption of CO on Pt surfaces was assumed as 420 μC cm^{-2}. The ORR polarization curves were measured in an O$_2$-saturated 0.1 M HClO$_4$ solution between 0.05 and 1.05 V$_{RHE}$ using a sweep rate of 10 mV s^{-1} at rotation rate of 1600 rpm. The accelerated durability tests (ADTs) were performed via cyclic sweeps between 0.6 and 1.1 V$_{RHE}$ in a O$_2$-saturated 0.1 M HClO$_4$ electrolyte at a sweep rate of 100 mV s^{-1} for different cycles.

3. Results and discussion

3.1. Synthesis and structural characterizations

The ultrathin Re-PtNiGa tetrametallic NWs were synthesized by using a facile wet-chemical method. The detailed structure and composition of the products were firstly analyzed. As shown in Fig. 1a, the low-magnification transmission electron microscopy (TEM) image distinctly shows the production of uniform and pure NWs. From the high-magnification TEM (Fig. 1b) and high-angle annular dark-field scanning TEM (HAADF-STEM) images (Fig. 1c), an average diameter of 0.98 ± 0.2 nm and length of 80 ± 26 nm could be estimated (inset in Fig. 1c). The atomic-level structural information was further reflected by the atomically resolved HAADF-STEM image of a single NW (Fig. 1d). Clearly, the thickness of NW was about five atomic layers, well consistent with the abovementioned average diameter. The measured lattice spacing of 0.19 nm and 0.23 nm can be assigned to the {200} and {111} planes, corresponding to the fast Fourier transform (FFT) pattern in the inset. From the distinguished lattice planes, we could deduce that the NWs grew along the direction of <110> orientation. The STEM energy dispersive spectroscopy (STEM-EDS) elemental mapping (Fig. 1e) and EDS line-scanning profile (Fig. 1f) together clearly indicate that Pt, Ni, Ga and Re elements are evenly distributed throughout the NWs. The atomic ratio of Pt/Ni/Ga/Re was quantitatively estimated to be 2.98:1.00:0.11:0.09 by inductively coupled plasma atomic emission spectroscopy (ICP-AES). The presence of Pt, Ni, Ga, and Re elements in
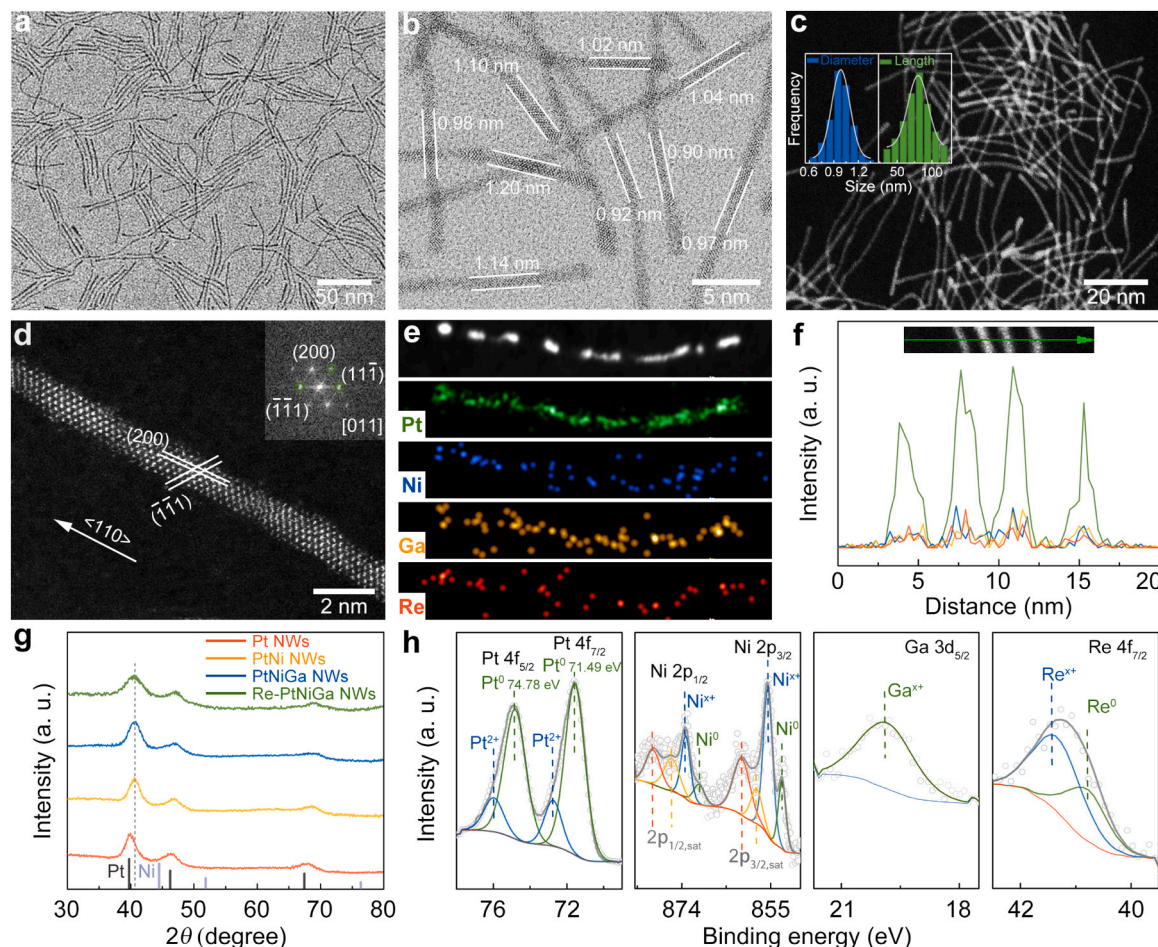

Fig. 1. Structural and compositional characterizations of one-nanometer-thick Re-PtNiGa NWs. (a) Low-magnification TEM image. (b) High-magnification TEM image. (c) HAADF-STEM image. The inset shows histogram of diameter and length distributions. (d) Atomically resolved HAADF-STEM image. The inset shows the corresponding FFT pattern. (e) STEM-EDS elemental mapping profiles. (f) EDS line-scanning profiles of Re-PtNiGa NWs. (g) XRD patterns of the NWs. (h) High-resolution XPS spectra of Pt 4f, Ni 2p, Ga 3d, and Re 4f.

NWs was also confirmed by X-ray photoelectron spectroscopy (XPS) survey spectrum (Fig. S1), with estimated Pt/Ni/Ga/Re atomic ratio of 3.03:1.00:0.09:0.07. Furthermore, the powder X-ray diffraction (PXRD) peaks of NWs present a shift toward high diffraction angle relative to those of pure Pt, consistent with the formation of Re-PtNiGa tetrametallic NWs considering the reduced lattice constant (Fig. 1g). The chemical states of the components in NWs were also disclosed by analyzing the high-resolution XPS spectra of Pt 4f, Ni 2p, Ga 3d and Re 4f (Fig. 1h). Specifically, most of the Pt displays a metallic Pt^0, while the majority of Ni, Ga and Re respectively present the oxidized states. The presence of oxidized Ni^{x+}, Ga^{x+} and Re^{x+} is probably related with the surface oxidation due to the feature of ultrathin diameter. These results together definitely demonstrate the formation of the one-nanometer-thick Re-PtNiGa tetrametallic NWs. It should be noted that this is the first work to achieve the doping of ETM Re into NWs to form one-nanometer-thin Re-PtNiGa tetrametallic NWs.

Besides, the microstructures and compositions of Pt, PtNi, and PtNiGa NWs were also characterized by TEM, EDS elemental mapping, and XPS (Figs. S2–S4). The TEM images clearly show the productions of uniform NWs with diameters ranging from 1.10 to 1.50 nm, demonstrating the ultrathin characteristic of NWs. The compositions of NWs were also verified by EDS elemental mapping profiles and XPS spectra. Furthermore, the atomic ratios of all Pt-based NWs were estimated based on the XPS analysis, as shown in Table S1. These structural and compositional characterizations together have evidenced the successful synthesis of Pt, PtNi, and PtNiGa NWs.

3.2. ORR activity of electrocatalysts

The electrocatalytic properties of the Re-PtNiGa tetrametallic NWs were then assessed toward ORR in acidic media. The ORR performance of PtNiGa trimetallic NWs, PtNi bimetallic NWs, Pt NWs, and commercial Pt/C catalyst were also compared under the identical condition. Before the measurements, various carbon-supported NW catalysts, which were then washed with acetic acid at 70 °C to clean the surfactants. As shown in Fig. S5, the infrared spectra of the catalysts indicate the removal of CTAB from the surface of NWs after the treatment. Also, the composition of Re-PtNiGa tetrametallic NWs was examined after the washing process by ICP-AES, showing the value slightly changing from 2.98:1.00:0.11:0.09 to 3.36:1.00:0.09:0.08. Fig. 2a shows the cyclic voltammograms (CVs) of the catalysts recorded at room temperature in a N$_2$-saturated 0.1 M HClO$_4$ solution at a sweep rate of 50 mV s^{-1}. From the region associated with hydrogen underpotential deposition (H$_{upd}$) in the potential range of 0.05–0.38 V$_{RHE}$, the electrochemically active surface area (ECSA) of each catalyst was then derived by assuming a charge density of 210 μC cm^{-2} for Pt. Specifically, the ECSAs of Re-PtNiGa NWs/C, PtNiGa NWs/C, PtNi NWs/C, Pt NWs/C, and commercial Pt/C catalysts were determined to be of 110.1 m^2 g^{-1}$_{Pt}$, 103.5 m^2 g^{-1}$_{Pt}$, 87.9 m^2 g^{-1}$_{Pt}$, 78.0 m^2 g^{-1}$_{Pt}$, and 63.3 m^2 g^{-1}$_{Pt}$, respectively, self-consistent with the trend in diameters of catalysts.

The electrocatalytic activities of various catalysts toward ORR were evaluated by recording the positive-going ORR polarization curves in O$_2$-saturated 0.1 M HClO$_4$ electrolyte with the rotating disk electrode (RDE) method. As shown in Fig. 2b, the Re-PtNiGa NWs/C catalyst exhibits the most positive half-wave potential, proving the best catalytic
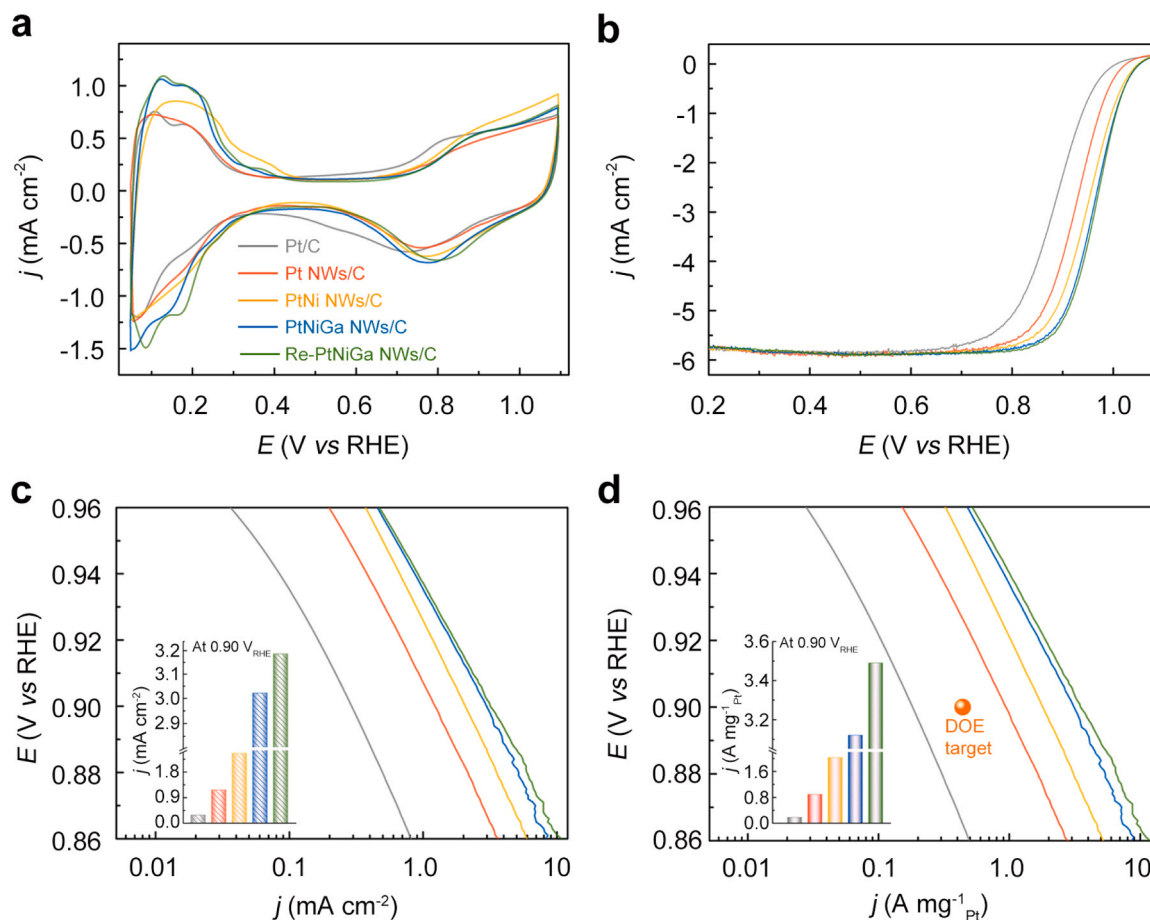

Fig. 2. Electrochemical properties of different catalysts. (a) CVs recorded at room temperature in N$_2$-saturated 0.1 M HClO$_4$ solutions at a sweep rate of 50 mV s^{-1}. (b) ORR polarization curves recorded at room temperature in O$_2$-saturated 0.1 M HClO$_4$ solutions at a sweep rate of 10 mV s^{-1} and a rotation rate of 1600 rpm. Tafel plots of (c) specific activity and (d) mass activity. The color scheme in (a) applies to all other panels.

activity toward ORR. For quantification, the specific activities (Fig. 2c) and mass activities (Fig. 2d) of the catalysts were then calculated by normalizing the kinetic currents, which were estimated based on the Koutecký-Levich equation, against the corresponding ECSA and Pt mass, respectively. At 0.9 V_{RHE}, the Re-PtNiGa tetrametallic NWs/C catalyst also shows the highest specific activity (3.17 mA cm^{-2} at 0.9 V_{RHE}), presenting 11.3-, 2.8-, 1.3-, and 1.1-fold enhancements relative to these of commercial Pt/C catalyst (0.28 mA cm^{-2}), Pt NWs/C catalyst (1.14 mA cm^{-2}), PtNi bimetallic NWs/C catalyst (2.40 mA cm^{-2}) and PtNiGa trimetallic NWs/C catalyst (3.01 mA cm^{-2}), respectively (Fig. 2c). Agreeing with the trend in specific activity, the Re-PtNiGa tetrametallic NWs/C catalyst displays the highest mass activity of 3.49 A mg$^{-1}_{Pt}$, which is 19.6, 3.9, 1.7, and 1.1 times greater than these of commercial Pt/C catalyst (0.18 A mg$^{-1}_{Pt}$), Pt NWs/C catalyst (0.89 A mg$^{-1}_{Pt}$), PtNi bimetallic NWs/C catalyst (2.11 A mg$^{-1}_{Pt}$) and PtNiGa trimetallic NWs/C catalyst (3.12 A mg$^{-1}_{Pt}$), respectively

(Fig. 2d). Remarkably, the mass activity of the Re-PtNiGa tetrametallic NWs/C catalyst is even 7.9 times higher than that of the value (0.44 A mg$^{-1}_{Pt}$ as marked in Fig. 2d) set as the 2020 targets by U.S. Department of Energy (DOE), indicating the great application potential for PEMFCs. Since 0.9 V_{RHE} is close to the diffusion-limited region in the polarization curve of Re-PtNiGa tetrametallic NWs/C catalyst [13,14, 43], we also calculated the mass activities and specific activities at 0.95 V_{RHE} for catalysts (Fig. S6).

3.3. Stability test

Since the catalytic durability is another key parameter to determine the application potential, we evaluated the long-term durability of these catalysts through an accelerated durability test (ADT) between 0.6 and 1.1 V_{RHE} in oxygen-saturated 0.1 M HClO$_4$ at a scan rate of 100 mV s^{-1}. As shown in Fig. 3a and b, the Re-PtNiGa tetrametallic catalyst presents
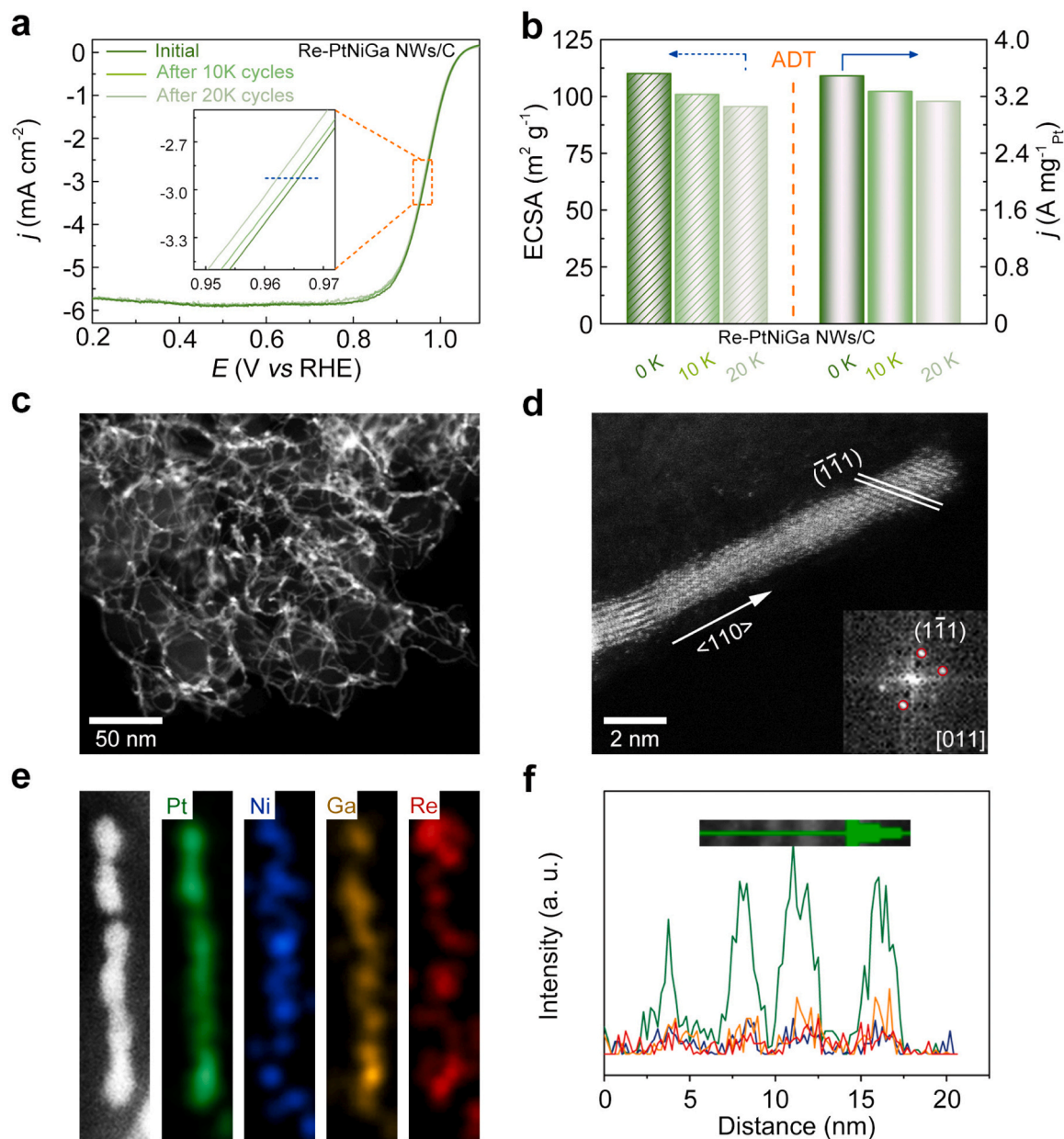

Fig. 3. Electrocatalytic durability and structural characterizations of Re-PtNiGa alloy NWs after 20 K cycles. (a) LSV curves before and after ADTs of different cycles. (b) The comparison of ECSA and mass activities at 0.9 V_{RHE} before and after ADTs of different cycles. (c) HAADF-STEM image. (d) Atomic-resolution HAADF-STEM image. The inset shows the corresponding FFT pattern. (e) STEM-EDS elemental mapping profiles. (f) STEM-EDS line-scanning profile.

the best durability with a 10.6% loss in mass activity after 20,000 cycles of ADTs, contrasting with a drop of 66.2% for commercial Pt/C catalyst (Fig. S7), 31.5% for Pt NWs/C catalyst (Fig. S8), 48.9% for PtNi bimetallic NWs/C catalyst (Fig. S9), and 16.0% for PtNiGa trimetallic NWs/C (Fig. S10). It should be mentioned herein that the remarkable overall performance (mass activity and durability) of the reported Re-PtNiGa NWs surpasses most of Appendix A the recently-reported Pt-based electrocatalysts (Fig. S11 and Table S2). Since the changes in ECSA and composition are the possible causes for the performance degradation, we further probed the ECSAs and compositions of catalysts after 20,000 cycles of ADTs to rationalize the best durability of Re-PtNiGa NWs/C catalyst. For Re-PtNiGa NWs/C catalyst, the ECSA only reduces by 12.8% (Fig. 3b), against a big loss of 69.7% for commercial Pt/C catalyst, 38.1% for Pt NWs/C catalyst, 52.5% for PtNi bimetallic NWs/C catalyst, and 17.1% for PtNiGa NWs/C catalyst (Figs. S7–S10). The observations in the morphologies of the catalysts after 20,000 cycles of ADTs also support the trend in ECSA loss (Figs. 3c and S12), which may be related with the favored surface reconstruction that exposes more active (111) facet. Specifically, the diameters of Pt, PtNi, PtNiGa NWs and Re-PtNiGa NWs increased from 1.5, 1.4, 1.0, 0.98 nm to 2.3, 2.5, 1.5, 1.2 nm, respectively (Fig. S13), well agreeing with the trend in ECSA loss. Meanwhile, we found that the Re-PtNiGa NWs/C catalysts well reserve its initial composition, with atomic ratio of Pt/Ni/Ga/Re changing from 3.36:1.00:0.09:0.08 to 3.87:1.00:0.11:0.12. Besides, the atomic structure of Re-PtNiGa NWs after ADTs was then determined by atomic-resolution HAADF-STEM image (Fig. 3d), which indicated its fcc phase and growth direction of <110> orientation, consistent with the FFT pattern showed in the inset. The well-reserved structure and composition of Re-PtNiGa NWs/C catalyst after 20,000 cycles of ADTs were further confirmed by the STEM elemental mapping and line scanning profiles shown in Fig. 3e and f, respectively. By contrast, the atomic ratio of Pt/Ni for PtNi NWs/C and Pt/Ni/Ga for PtNiGa NWs/C catalyst changes from 2.95:1.00 and 3.42:1.00:0.10 to 10.30:1.00 and 4.19:1.00:0.11, respectively, hinting the severe leaching of Ni during the ADTs. Based on the above results, we thus believe that the stable structure and composition of the Re-PtNiGa NWs during the ADTs are responsible for the outstanding durability. From the above results, we could conclude that the incorporation of ETM Re elements into PtNiGa NWs boosts the ORR activity and durability.

3.4. Membrane electrodes assembly (MEA) performance

Inspired by the outstanding ORR performance of Re-PtNiGa tetrametallic NWs/C catalyst, we further also estimated the membrane electrodes assembly (MEA) performance, while Re-PtNiGa NWs/C catalyst was also corroborated by incorporating the catalyst on the cathode of MEA with a Pt loading amount of 0.14 mg cm^{-2} in a real H$_2$-O$_2$ PEMFC. For a comparison, the PtNiGa NWs/C and commercial Pt/C catalysts on the cathode of MEA with a Pt loading amount of 0.15 mg cm^{-2} and 0.16 mg cm^{-2} were also measured, respectively. As shown in Fig. 4a, the Re-PtNiGa NWs/C catalyst displayed the greatest activity in MEA, with the highest maximum power density and (961 mW cm^{-2}) than those of PtNiGa NWs/C (830 mW cm^{-2}) and commercial Pt/C catalysts (702 mW cm^{-2}). The mass activity at 0.9 V and current density at 0.8 V of Re-PtNiGa NWs/C was slightly lower than that of DOE target, which may be attributed to the difference in test conditions and process technology. Given the identical test conditions for three catalysts, the highest power density, mass activity (0.9 V), and current density (0.8 V) can be rationally ascribed to the improved ORR activity of Re-PtNiGa NWs/C catalyst, strongly supporting the boosted ORR activity. In addition, the assembled H$_2$-O$_2$ PEMFC exhibit an excellent long-term durability, showing a negligible decay (4.9%) of the output current density at a discharge voltage of 0.75 V for 100 h (Fig. 4b). Definitely, such remarkable MEA activity and stability of the Re-PtNiGa tetrametallic NWs/C catalyst prove the great potential of the PEMECs.

3.5. Density functional theory (DFT) calculations

We further performed density functional theory (DFT) calculations to demonstrate the observed experimental results in activity and stability for catalysts. Before the modeling, the values of ECSA (CO stripping)/ ECSA (HUPD) are both close to 1.5 (Fig. S15) [42], which imply the formation of Pt-skin structures for PtNi NWs/C, PtNiGa NWs/C and Re-PtNiGa NWs/C catalysts (treated with acetic acid). Since the {111} surface facets are thermodynamically favored under the ORR measurement condition [7,44–48], Re-PtNiGa (111) slab, PtNiGa (111) slab and PtNi (111) slab with Pt-skin structure and the close compositions were constructed as the models to represent the Re-PtNiGa NWs/C, PtNiGa NWs/C and PtNi NWs/C catalysts, respectively (Fig. 5a and S16). Also, the Pt (111) slab was constructed for Pt NWs/C catalyst (Fig. S16). The Gibbs free energies of intermediates on different slabs were then calculated by DFT to gain the intrinsic understanding. As shown in Fig. 5b, the desorption of hydroxyl from the catalysts was determined as the rate-limiting step due to the too strong binding of hydroxyl, consistent with previous studies on Pt-based ORR electrocatalysts [23, 49–51]. The overpotentials for ORR on the Pt (111), PtNi (111), PtNiGa (111) and Re-PtNiGa (111) slabs were then estimated at 0.63 V, 0.50 V, 0.49 V and 0.44 V from the energy diagram (Fig. S17), respectively, self-supporting the trend in catalytic activity for the catalysts. It is noted
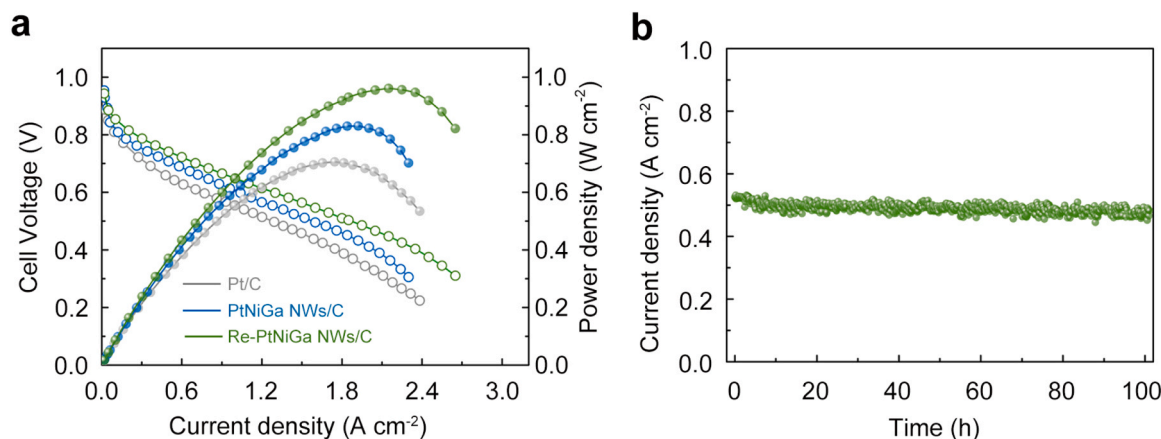

Fig. 4. Fuel-cell performance of various catalysts. (a) H$_2$–O$_2$ fuel cell i–V polarization plots of prepared MEAs with the cathode Pt loading of 0.14 mg$_{Pt}$ cm^{-2} for Re-PtNiGa/C, 0.15 mg$_{Pt}$ cm^{-2} for PtNiGa NWs/C, and 0.16 mg$_{Pt}$ cm^{-2} for commercial Pt/C. (b) Current density plot as the function of operating time for MEA with Re-PtNiGa/C as the cathode catalyst at a constant fuel cell voltage of 0.75 V.
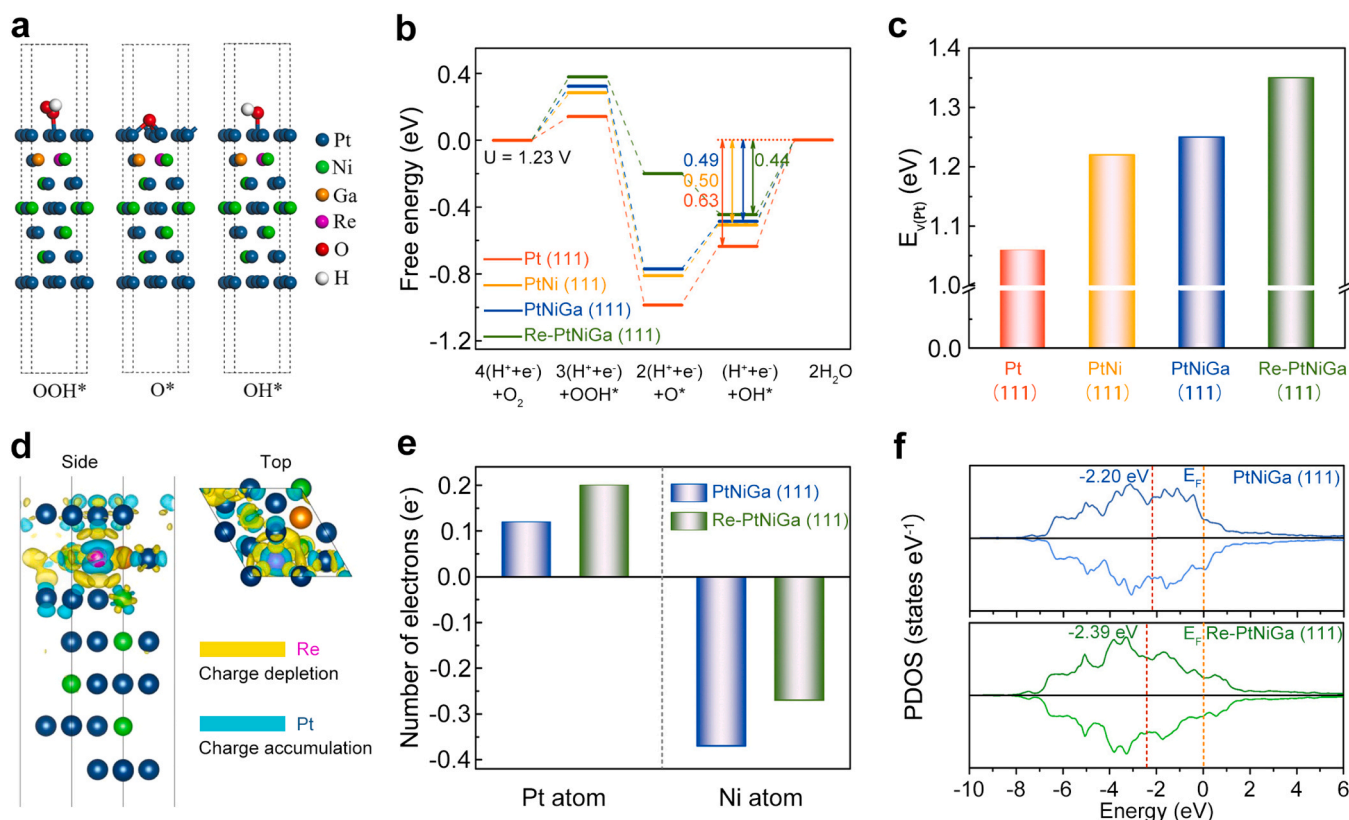
Fig. 5. DFT calculations. (a) The adsorbed intermediate configurations for ORR on Re-PtNiGa tetrametallic NWs. (b) The calculated free energy diagrams at the equilibrium potential (U = 1.23 V). (c) Pt vacancy formation energies ($E_{V(Pt)}$) for different slabs. (d) The differential charge distributions for Re-PtNiGa alloy slab. (e) The total amount of electrons for surface Pt and subsurface Ni atoms of various NWs. (f) The plots of projected d-density of states (PDOS) of surface Pt atoms for PtNiGa and Re-PtNiGa alloy slabs.

that the optimized Re-PtNiGa (111), PtNiGa (111) and PtNi (111) slabs show 1.3% compressed lattice constant relative to Pt (111) slab due to the smaller radius of Ni atoms. Besides, the ligand effect is caused by the electronic charge transfer between dissimilar atoms with different electronegativities, which further impacts the electronic band structure and thus regulates the catalytic activity. Taken the analysis together, the intrinsic compressive strain and ligand effect would reduce the binding strength of hydroxyl, which leads to the lower overpotential of PtNi (111) slab compared to Pt (111) slab [16,52]. In addition, the Re-PtNiGa (111) slab presents the vacancy formation energy ($E_{V(Pt)}$), a descriptor for the stability of Pt-based catalysts [32,53], that is significantly larger than that of other comparison slabs (Fig. 5c). These results together indicate a high degree of consistency with the experimental observations in terms of activity and durability for ORR.

Besides, we provided the in-depth insights into the effects of the incorporated ETM Re on the electronic structure, which intrinsically determines the catalytic performance. We first analyzed the partial projected d-density of states (PDOS) of Re-PtNiGa slab, indicating existence of strong interaction between Pt and Re, as shown in Fig. S18. Subsequently, the differential charge analysis of Re-PtNiGa surface shown in Fig. 5d revealed that the electrons accumulate around Pt atoms, while the surrounding of Re atom possesses charge depletion, indicating that the doping of Re caused the transfer of electrons from Re to Pt in the Re-PtNiGa NWs. In fact, the negative shift of Pt 4f peaks in Re-PtNiGaW NWs (Fig. 1h) compared with the PtNiGa NWs (Fig. S4e) and the Bader charge analysis further confirmed the electron transfer from Re to neighboring Pt and Ni atoms [54], as shown in Fig. 5e. Indeed, the electron-rich Pt and Ni sites Re-PtNiGa NWs could result in the elevated dissolution potential, consistent with the calculations in Fig. 5c. Basically, the electronic charge transfer between dissimilar atoms with different electronegativities could impact the electronic

band structure and thus regulate the catalytic activity. Moreover, according to the d-band theory, the binding interaction between adsorbates and catalysts plays a critical role to assess ORR activity. Correspondingly, PDOS of Re-PtNiGa (111) slab and PtNiGa (111) slab are shown in Fig. 5f, indicating that the dopant Re caused a deeper d-band center below the Fermi level (E_F). The downward shift of d-band center is also directly supported by the variations in d-band centers of the catalysts characterized with XPS surface valence band (Fig. S19). These results manifest the weakened binding strength between intermediate oxygen species and Pt for Re-PtNiGa NWs and thus signify an improved ORR activity. Overall, the ETM Re dopants could donate the electrons to Pt atoms, which optimize the electronic band structure of Pt site and thus improving both activity and durability of the Re-PtNiGa NWs/C catalyst.

4. Conclusion

In summary, we have realized the trace doping of ETM Re into ultrathin PtNiGa NWs, which integrated the superior activity, long-time durability, and high utilization efficiency of Pt atoms into one catalyst. Remarkably, the Re-PtNiGa tetrametallic NWs present 19.6 and 11.3-fold enhancements in mass activity and specific activity compared to commercial Pt/C catalyst, respectively. Besides, the Re-PtNiGa tetrametallic NWs exhibit a 10.6% loss in mass activity after 20,000 cycles of ADTs. The excellent ORR activity and durability of Re-PtNiGa tetrametallic NWs were also solidly confirmed by the great performance of the assembled fuel cell. The DFT calculations revealed the weakened binding strength of oxygenated species and improved dissolution potential due to the advantageous synergies between optimal electronic structure and unique structure of Re-PtNiGa NWs accounted for the great enhancements. We believe that the present work not only provides

a remarkable ORR catalyst to advance the commercialization of fuel cells but also demonstrates the ETM-doped strategy is an effective method to optimize the heterogeneous catalysts.

CRediT authorship contribution statement

Lei Gao: Investigation, Methodology, Data curation, Writing – original draft. **Tulai Sun:** Software, Data curation. **Xin Tan:** Software, Data curation, Funding acquisition. **Maochang Liu:** Supervision, Data curation. **Fei Xue:** Methodology, Data curation. **Bin Wang:** Conceptualization, Data curation. **Jiawei Zhang:** Investigation, Data curation, Funding acquisition. **Yang-Fan Lu:** Software, Data curation. **Chao Ma:** Software, Data curation. **He Tian:** Supervision, Data curation. **Shengchun Yang:** Conceptualization, Data curation. **Sean C. Smith:** Software, Data curation, Funding acquisition. **Hongwen Huang:** Conceptualization, Supervision, Project administration, Funding acquisition, Writing – review & editing.

Lei Gao: Performed the sample synthesis, carried out the electrochemical measurements, and analyzed the experimental data. **Tulai Sun, Chao Ma, and He Tian:** Performed the HAADF-STEM characterizations and analyzed the data. **Xin Tan and Sean C. Smith:** Conducted the DFT simulation and theoretical analyses. **Jiawei Zhang and Shengchun Yang:** Helped with the analysis and discussion of experimental data. **Fei Xue:** performed the XRD and FTIR measurements. **Yang-Fan Lu:** Performed the XPS experiments. **Bin Wang, Maochang Liu, and Hongwen Huang:** Conceived the idea and wrote the manuscript. All the authors were involved in the discussion and analysis of the manuscript.

Declaration of Competing Interest

The authors declare that they have no known competing financial interests or personal relationships that could have appeared to influence the work reported in this paper.

Acknowledgment

Appendix A. Supplementary material

Supplementary data associated with this article can be found in the online version at doi:10.1016/j.apcatb.2021.120918.

References

[1] H.A. Gasteiger, N.M. Marković, Just a dream—or future reality? Science 324 (2009) 48–49.

[2] M. Shao, Q. Chang, J.-P. Dodelet, R. Chenitz, Recent advances in electrocatalysts for oxygen reduction reaction, Chem. Rev. 116 (2016) 3594–3657.

[3] J. Zhang, Y. Yuan, L. Gao, G. Zeng, M. Li, H. Huang, Stabilizing Pt-based electrocatalysts for oxygen reduction reaction: fundamental understanding and design strategies, Adv. Mater. 33 (2021) 2006494.

[4] X.X. Wang, M.T. Swihart, G. Wu, Achievements, challenges and perspectives on cathode catalysts in proton exchange membrane fuel cells for transportation, Nat. Catal. 2 (2019) 578–589.

[5] M. Liu, Z. Zhao, X. Duan, Y. Huang, Nanoscale structure design for high-performance Pt-based ORR catalysts, Adv. Mater. 31 (2019), 1802234.

[6] J. Wu, H. Yang, Platinum-based oxygen reduction electrocatalysts, Acc. Chem. Res. 46 (2013) 1848–1857.

[7] V.R. Stamenkovic, B. Fowler, B.S. Mun, G. Wang, P.N. Ross, C.A. Lucas, N. M. Markovic, Improved oxygen reduction activity on Pt₃Ni (111) via increased surface site availability, Science 315 (2007) 493–497.

[8] L. Zhang, L.T. Roling, X. Wang, M. Vara, M. Chi, J. Liu, S.-I. Choi, J. Park, J. A. Herron, Z. Xie, M. Mavrikakis, Y. Xia, Platinum-based nanocages with subnanometer-thick walls and well-defined, controllable facets, Science 349 (2015) 412–416.

[9] X. Wang, S.I. Choi, L.T. Roling, M. Luo, C. Ma, L. Zhang, M. Chi, J. Liu, Z. Xie, J. A. Herron, M. Mavrikakis, Y. Xia, Palladium-platinum core-shell icosahedra with substantially enhanced activity and durability towards oxygen reduction, Nat. Commun. 6 (2015) 7954.

[10] X. Li, X. Li, C. Liu, H. Huang, P. Gao, F. Ahmad, L. Luo, Y. Ye, Z. Geng, G. Wang, R. Si, C. Ma, J. Yang, J. Zeng, Atomic-level construction of tensile-strained PdFe alloy surface toward highly efficient oxygen reduction electrocatalysis, Nano Lett. 20 (2020) 1403–1409.

[11] D.Y. Chung, S. Park, H. Lee, H. Kim, Y.-H. Chung, J.M. Yoo, D. Ahn, S.-H. Yu, K.-S. Lee, M. Ahmadi, H. Ju, H.D. Abruña, S.J. Yoo, B.S. Mun, Y.-E. Sung, Activity–stability relationship in Au@Pt nanoparticles for electrocatalysis, ACS Energy Lett. 5 (2020) 2827–2834.

[12] J. Guo, L. Gao, X. Tan, Y. Yuan, J. Kim, Y. Wang, H. Wang, Y.-J. Zeng, S.-I. Choi, C. Smith, H. Huang, Template-directed rapid synthesis of Pd-based ultrathin porous intermetallic nanosheets for efficient oxygen reduction, Angew. Chem. Int. Ed. 60 (2021) 10942–10949.

[13] H. Kwon, M.K. Kabiraz, J. Park, A. Oh, H. Baik, S.-I. Choi, K. Lee, Dendrite-embedded platinum-nickel multiframes as highly active and durable electrocatalyst toward the oxygen reduction reaction, Nano Lett. 18 (2018) 2930–2936.

[14] C. Chen, Y. Kang, Z. Huo, Z. Zhu, W. Huang, H.L. Xin, J.D. Snyder, D. Li, J. A. Herron, M. Mavrikakis, M. Chi, K.L. More, Y. Li, N.M. Markovic, G.A. Somorjai, P. Yang, V.R. Stamenkovic, Highly crystalline multimetallic nanoframes with three-dimensional electrocatalytic surfaces, Science 343 (2014) 1339–1343.

[15] G.-R. Zhang, S. Wöllner, Hollowed structured PtNi bifunctional electrocatalyst with record low total overpotential for oxygen reduction and oxygen evolution reactions, Appl. Catal. B: Environ. 222 (2018) 26–34.

[16] K. Li, X. Li, H. Huang, L. Luo, X. Li, X. Yan, C. Ma, R. Si, J. Yang, J. Zeng, One-nanometer-thick PtNiRh trimetallic nanowires with enhanced oxygen reduction electrocatalysis in acid media: integrating multiple advantages into one catalyst, J. Am. Chem. Soc. 140 (2018) 16159–16167.

[17] H. Huang, A. Ruditskiy, S.-I. Choi, L. Zhang, J. Liu, Z. Ye, Y. Xia, One-pot synthesis of penta-twinned palladium nanowires and their enhanced electrocatalytic properties, ACS Appl. Mater. Interfaces 9 (2017) 31203–31212.

[18] M. Escudero-Escribano, P. Malacrida, M.H. Hansen, U.G. Vej-Hansen, A. Velázquez-Palenzuela, V. Tripkovic, J. Schiøtz, J. Rossmeisl, I.E.L. Stephens, I. Chorkendorff, Tuning the activity of Pt alloy electrocatalysts by means of the lanthanide contraction, Science 352 (2016) 73–76.

[19] J. Li, H.-M. Yin, X.-B. Li, E. Okunishi, Y.-L. Shen, J. He, Z.-K. Tang, W.-X. Wang, E. Yücelen, C. Li, Y. Gong, L. Gu, S. Miao, L.-M. Liu, J. Luo, Y. Ding, Surface evolution of a Pt-Pd-Au electrocatalyst for stable oxygen reduction, Nat. Energy 2 (2017) 17111.

[20] J. Li, Z. Xi, Y.-T. Pan, J.S. Spendelow, P.N. Duchesne, D. Su, Q. Li, C. Yu, Z. Yin, B. Shen, Y.S. Kim, P. Zhang, S. Sun, Fe stabilization by intermetallic L1₀-FePt and Pt catalysis enhancement in L1₀-FePt/Pt nanoparticles for efficient oxygen reduction reaction, J. Am. Chem. Soc. 140 (2018) 2926–2932.

[21] M. Gong, D. Xiao, Z. Deng, R. Zhang, W. Xia, T. Zhao, X. Liu, T. Shen, Y. Hu, Y. Lu, X. Zhao, H. Xin, D. Wang, Structure evolution of PtCu nanoframes from disordered to ordered for the oxygen reduction reaction, Appl. Catal. B: Environ. 282 (2020), 119617.

[22] J. Liang, N. Li, Z. Zhao, L. Ma, X. Wang, S. Li, X. Liu, T. Wang, Y. Du, G. Lu, J. Han, Y. Huang, D. Su, Q. Li, Tungsten-doped L1₀-PtCo ultrasmall nanoparticles as high-performance fuel cell cathode, Angew. Chem. Int. Ed. 131 (2019) 15617–15623.

[23] J. Greeley, I.E.L. Stephens, A.S. Bondarenko, T.P. Johansson, H.A. Hansen, T. F. Jaramillo, J. Rossmeisl, I. Chorkendorff, J.K. Nørskov, Alloys of platinum and early transition metals as oxygen reduction electrocatalysts, Nat. Chem. 1 (2009) 552–556.

[24] F. Ahmad, L. Luo, X. Li, H. Huang, J. Zeng, Boosting fuel cell catalysis by surface doping of W on Pd nanocubes, Chin. J. Catal. 39 (2018) 1202–1209.

[25] M.K. Kabiraz, J. Kim, S.-I. Choi, Shape and hydriding effects of palladium nanocatalyst toward oxygen electroreduction reaction, Bull. Korean Chem. Soc. 42 (2021) 802–805.

[26] J. Lim, H. Shin, M. Kim, H. Lee, K.-S. Lee, Y. Kwon, D. Song, S. Oh, H. Kim, E. Cho, Ga–doped Pt–Ni octahedral nanoparticles as a highly active and durable electrocatalyst for oxygen reduction reaction, Nano Lett. 18 (2018) 2450–2458.

[27] L. Gao, X. Li, Z. Yao, H. Bai, Y. Lu, C. Ma, S. Lu, Z. Peng, J. Yang, A. Pan, H. Huang, Unconventional p–d hybridization interaction in PtGa ultrathin nanowires boosts oxygen reduction electrocatalysis, J. Am. Chem. Soc. 141 (2019) 18083–18090.

[28] C. Wang, Y. Hou, J. Kim, S. Sun, A general strategy for synthesizing FePt nanowires and nanorods, Angew. Chem., Int. Ed. 46 (2007) 6333–6335.

[29] M. Li, Z. Zhao, T. Cheng, A. Fortunelli, C.-Y. Chen, R. Yu, Q. Zhang, L. Gu, B. V. Merinov, Z. Lin, E. Zhu, T. Yu, Q. Jia, J. Guo, L. Zhang, W.A. Goddard III, Y. Huang, X. Duan, Ultrafine jagged platinum nanowires enable ultrahigh mass activity for the oxygen reduction reaction, Science 354 (2016) 1414–1419.

[30] K. Jiang, D. Zhao, S. Guo, X. Zhang, X. Zhu, J. Guo, G. Lu, X. Huang, Efficient oxygen reduction catalysis by subnanometer Pt alloy nanowires, Sci. Adv. 3 (2017), e1601705.

[31] X. Fan, S. Luo, X. Zhao, X. Wu, Z. Luo, M. Tang, W. Chen, X. Song, Z. Quan, One-nanometer-thick platinum-based nanowires with controllable surface structures, Nano Res. 12 (2019) 1721–1726.

[32] H. Huang, K. Li, Z. Chen, L. Luo, Y. Gu, D. Zhang, C. Ma, R. Si, J. Yang, Z. Peng, J. Zeng, Achieving remarkable activity and durability toward oxygen reduction reaction based on ultrathin Rh-doped Pt nanowires, J. Am. Chem. Soc. 139 (2017) 8152–8159.

[33] J. Kim, M.K. Kabiraz, W. Lee, G.H. Hwang, S.-I. Choi, Solvothermal doping of lanthanum on nanoscale platinum surfaces to improve oxygen electroreduction performance, ChemElectroChem 7 (2020) 2643–2650.

[34] Z. Kong, Y. Maswadeh, J.A. Vargas, S. Shan, Z.-P. Wu, H. Kareem, A.C. Leff, D. T. Tran, F. Chang, S. Yan, S. Nam, X. Zhao, J.M. Lee, J. Luo, S. Shastri, G. Yu, V. Petkov, C.-J. Zhong, Origin of high activity and durability of twisty nanowire alloy catalysts under oxygen reduction and fuel cell operating conditions, J. Am. Chem. Soc. 142 (2020) 1287–1299.

[35] M. Luo, Y. Sun, X. Zhang, Y. Qin, M. Li, Y. Li, C. Li, Y. Yang, L. Wang, P. Gao, G. Lu, S. Guo, Stable high-index faceted Pt skin on zigzag-like PtFe nanowires enhances oxygen reduction catalysis, Adv. Mater. 30 (2018), 1705515.

[36] X. Tian, X. Zhao, Y.-Q. Su, L. Wang, H. Wang, D. Dang, B. Chi, H. Liu, E.J. M. Hensen, X.W. Lou, B.Y. Xia, Engineering bunched Pt-Ni alloy nanocages for efficient oxygen reduction in practical fuel cells, Science 366 (2019) 850–856.

[37] J. Mao, W. Chen, D. He, J. Wan, J. Pei, J. Dong, Y. Wang, P. An, Z. Jin, W. Xing, H. Tang, Z. Zhuang, X. Liang, Y. Huang, G. Zhou, L. Wang, D. Wang, Y. Li, Design of ultrathin Pt-Mo-Ni nanowire catalysts for ethanol electrooxidation, Sci. Adv. 3 (2017), e1603068.

[38] L. Huang, M. Wei, N. Hu, P. Tsiakaras, P.K. Shen, Molybdenum-modified and vertex-reinforced quaternary hexapod nano-skeletons as efficient electrocatalysts for methanol oxidation and oxygen reduction reaction, Appl. Catal. B: Environ. 258 (2019), 117974.

[39] N.E. Sahin, T.W. Napporn, L. Dubau, F. Kadirgan, J.-M. Léger, K.B. Kokoh, Temperature-dependence of oxygen reduction activity on Pt/C and PtCr/C electrocatalysts synthesized from microwave-heated diethylene glycol method, Appl. Catal. B: Environ. 203 (2017) 72–84.

[40] S. Ghoshal, Q. Jia, M.K. Bates, J. Li, C. Xu, K. Gath, J. Yang, J. Waldecker, H. Che, W. Liang, G. Meng, Z.-F. Ma, S. Mukerjee, Tuning Nb–Pt interactions to facilitate fuel cell electrocatalysis, ACS Catal. 7 (2017) 4936–4946.

[41] D.A. Simonetti, E.L. Kunkes, J.A. Dumesic, Gas-phase conversion of glycerol to synthesis gas over carbon-supported platinum and platinum–rhenium catalysts, J. Catal. 247 (2007) 298–306.

[42] A. Naor, N. Eliaz, E. Gileadi, Electrodeposition of rhenium–nickel alloys from aqueous solutions, Electrochim. Acta 54 (2009) 6028–6035.

[43] M. Luo, Z. Zhao, Y. Zhang, Y. Sun, Y. Xing, F. Lv, Y. Yang, X. Zhang, S. Hwang, Y. Qin, J.-Y. Ma, F. Lin, D. Su, G. Lu, S. Guo, PdM bimetallene for oxygen reduction catalysis, Nature 574 (2019) 81–85.

[44] N. Becknell, Y. Kang, C. Chen, J. Resasco, N. Kornienko, J. Guo, N.M. Markovic, G. A. Somorjai, V.R. Stamenkovic, P. Yang, Atomic structure of Pt₃Ni nanoframe electrocatalysts by in situ X-ray absorption spectroscopy, J. Am. Chem. Soc. 137 (2015) 15817–15824.

[45] Y. Hu, J.O. Jensen, L.N. Cleemann, B.A. Brandes, Q. Li, Synthesis of Pt–rare earth metal nanoalloys, J. Am. Chem. Soc. 142 (2020) 953–961.

[46] D.F. van der Vliet, C. Wang, D. Tripkovic, D. Strmcnik, X.F. Zhang, M.K. Debe, R. T. Atanasoski, N.M. Markovic, V.R. Stamenkovic, Mesostructured thin films as electrocatalysts with tunable composition and surface morphology, Nat. Mater. 11 (2012) 1051–1058.

[47] C.H. Cui, L. Gan, M. Heggen, S. Rudi, P. Strasser, Compositional segregation in shaped Pt alloy nanoparticles and their structural behaviour during electrocatalysis, Nat. Mater. 12 (2013) 765–771.

[48] Y. Xu, A.V. Ruban, M. Mavrikakis, Adsorption and dissociation of O₂ on Pt–Co and Pt–Fe alloys, J. Am. Chem. Soc. 126 (2004) 4717–4725.

[49] V.R. Stamenkovic, B.S. Mun, M. Arenz, K.J.J. Mayrhofer, C.A. Lucas, G. Wang, P. N. Ross, N.M. Markovic, Trends in electrocatalysis on extended and nanoscale Pt-bimetallic alloy surfaces, Nat. Mater. 6 (2007) 241–247.

[50] V. Viswanathan, H.A. Hansen, J. Rossmeisl, J.K. Norskov, Universality in oxygen reduction electrocatalysis on metal surfaces, ACS Catal. 2 (2012) 1654–1660.

[51] Y. Jiao, Y. Zheng, M. Jaroniecb, S.Z. Qiao, Design of electrocatalysts for oxygen- and hydrogen- involving energy conversion reactions, Chem. Soc. Rev. 44 (2015) 2060–2086.

[52] D.Y. Chung, S.W. Jun, G. Yoon, S.G. Kwon, D.Y. Shin, P. Seo, J.M. Yoo, H. Shin, Y.-H. Chung, H. Kim, B.S. Mun, K.-S. Lee, N.-S. Lee, S.J. Yoo, D.-H. Lim, K. Kang, Y.-E. Sung, T. Hyeon, Highly durable and active PtFe nanocatalyst for electrochemical oxygen reduction reaction, J. Am. Chem. Soc. 137 (2015) 15478–15485.

[53] K. Ding, D.A. Cullen, L. Zhang, Z. Cao, A.D. Roy, I.N. Ivanov, D. Cao, A general synthesis approach for supported bimetallic nanoparticles via surface inorganometallic chemistry, Science 362 (2018) 560–564.

[54] W. Tang, E. Sanville, G. Henkelman, A grid-based bader analysis algorithm without lattice bias, J. Phys. Condens. Matter 21 (2009), 084204.